

# Two-Photon Interference of Photons from Remote Tin-Vacancy Centers in Diamond

Vladislav Bushmakin,<sup>1,2,\*</sup> Oliver von Berg,<sup>1</sup> Colin Sauerzapf,<sup>1</sup> Sreehari Jayaram,<sup>1</sup> Andrej Denisenko,<sup>1</sup> Cristina Tarín,<sup>3</sup> Jens Anders,<sup>4</sup> Vadim Vorobyov,<sup>1</sup> Ilja Gerhardt,<sup>5</sup> Di Liu,<sup>1,6</sup> and Jörg Wrachtrup<sup>1,2</sup>

<sup>1</sup>*3. Physikalisches Institut, Universität Stuttgart, Stuttgart 70569, Germany*

<sup>2</sup>*Max Planck Institute for Solid State Research, Stuttgart 70569, Germany*

<sup>3</sup>*Institute for System Dynamics, Universität Stuttgart, Stuttgart 70563, Germany*

<sup>4</sup>*Institute of Smart Sensors, Universität Stuttgart, Stuttgart 70569, Germany*

<sup>5</sup>*Institut für Festkörperphysik, Leibniz Universität Hannover, Hannover 30167, Germany*

<sup>6</sup>*John A. Paulson School of Engineering and Applied Sciences, Harvard University, Cambridge, MA 02138, USA*

Scalable quantum networks rely on optical connections between long-lived qubits to distribute entanglement. Tin vacancies in diamond have emerged as promising qubits, offering extended spin coherence times at liquid helium temperatures and spin-dependent, highly coherent optical transitions for effective photon-based communication. Connecting remote nodes requires quantum interference of indistinguishable photons, which is challenging in an inhomogeneous solid-state environment. Here, we demonstrate a two-node experiment with tin vacancies in diamond, which exhibit a resonant frequency distribution spanning approximately 8 GHz. To overcome the frequency mismatch, we tune the resonant frequencies of one node using the Stark effect. We achieve tunability up to 4 GHz while maintaining optical coherence. As a demonstration, we achieve detuning-dependent remote two-photon interference between separate nodes, obtaining 80(6) % interference visibility without postprocessing when the defects' optical transitions are tuned into resonance, and 63(8) % with detuning up to 20 times their natural linewidths. These results highlight the potential of tin-vacancy centres in diamond for establishing robust optical links between remote quantum registers.

## I. INTRODUCTION

Developing scalable quantum networks, where local quantum processing nodes are interconnected via indistinguishable photons, remains a central challenge in quantum information science [1]. Reliable optical links must be efficiently interfaced with quantum memories for such networks to function. Significant progress has been achieved with various platforms, including trapped atoms and ions [2–7], quantum dots [8, 9], organic molecules [10], rare-earth-doped solids [11, 12], transmon qubits [13], and solid-state defects [14–18]. Among these systems, color centers in diamond have emerged as promising candidates for scalable quantum applications due to their compatibility with nanophotonic devices [19, 20] and their long spin coherence times [21, 22]. Group-IV vacancy centers in diamond, such as the silicon-vacancy ( $\text{SiV}^-$ ) centre, offer distinct advantages owing to their inversion symmetry [23, 24], which renders them less sensitive to electric field fluctuations. This property enables integration into nanostructures without degrading optical coherence [25].  $\text{SiV}^-$  centers have demonstrated narrow inhomogeneous distributions, Fourier-limited linewidths [26, 27], and stable optical transitions, facilitating two-photon interference experiments between remote emitters [28, 29]. However,  $\text{SiV}^-$  centers suffer from low quantum efficiency and require operation at sub-Kelvin temperatures to achieve long spin coherence times [30, 31], which is impractical for scalable quantum networks.

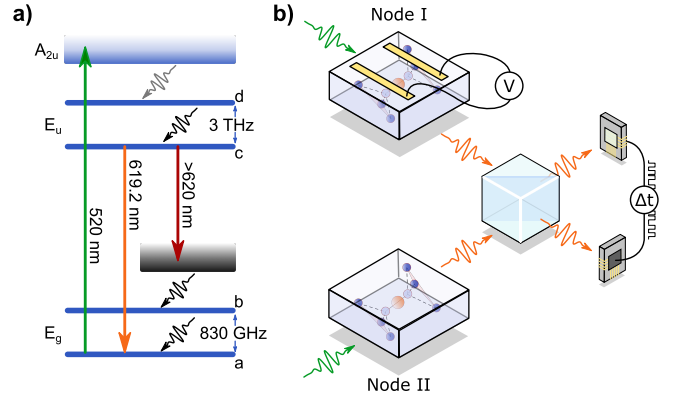


FIG. 1. (a) Energy level diagram for the negatively charged tin-vacancy ( $\text{SnV}^-$ ) centre in diamond, illustrating the electronic ground and excited states with their respective orbital splittings. The c-a transition (619.2 nm) between the lowest orbital levels is used in this experiment. (b) Concept of the remote two-photon experiment with one of the nodes tuned with an electric field.

Heavier group-IV defects, such as germanium-vacancy ( $\text{GeV}^-$ ), tin-vacancy ( $\text{SnV}^-$ ), and lead-vacancy ( $\text{PbV}^-$ ) centers, offer enhanced properties, including higher quantum efficiency, larger spin-orbit splitting, and longer spin relaxation times at elevated temperatures [32–36]. Notably, the  $\text{SnV}^-$  (see energy level diagram in Figure 1a) centre has demonstrated spin-lattice relaxation times  $T_1$  reaching 1 s at temperatures above 1 K and coherence times  $T_2$  extending up to 10 ms with dynamical decoupling [37–39]. Moreover, scalable integration of these centers onto CMOS-compatible photonic chips further

\* v.bushmakin@pi3.uni-stuttgart.de

positions the  $\text{SnV}^-$  centre as a promising candidate for quantum networking applications at practical temperatures [40].

Despite these promising characteristics, it remains challenging to achieve high optical coherence to perform two-photon interference with  $\text{SnV}^-$  centers. In solid-state environments like diamond, variations in the local environment surrounding each defect lead to inhomogeneous broadening — a spread in the distribution of the defects' zero-phonon line (ZPL) frequencies. For  $\text{SnV}^-$  centers, the larger atomic size of the tin ion exacerbates spectral broadening, as implantation-induced vacancies can introduce significant lattice strain and electric fields, resulting in broad ZPL distributions ranging from tens to hundreds of gigahertz [34]. Recent studies have demonstrated that it is possible to reduce the inhomogeneous broadening of  $\text{SnV}^-$  centers to approximately 4 GHz by employing HPHT annealing [41]. Although this improvement marks significant progress, the reduced inhomogeneous broadening still remains over 130 times larger than the natural linewidth, making it extremely unlikely to find two defects with overlapping emission frequencies for interference experiments. Consequently, tuning mechanisms are required to bring individual  $\text{SnV}^-$  centers into resonance. Previous efforts to tune optical transitions through application of electric fields have been limited, as they cause significant spectral diffusion [42, 43]. Spectral diffusion degrades the optical coherence necessary for high-visibility two-photon interference, presenting a significant obstacle to utilizing  $\text{SnV}^-$  centers in scalable quantum networks.

In this work, we address the challenges of achieving high optical coherence and performing two-photon interference with  $\text{SnV}^-$  centers with the diamond chips in two remote optical setups separated by 70 meters of optical fiber (Node I and Node II, depicted conceptually in Figure 1b and in detail in Figure 3a). We create  $\text{SnV}^-$  centers in diamond with low strain and a narrow inhomogeneous distribution. By implementing Stark tuning of optical transitions with minimal decoherence, we bring the optical transitions of separate defects into resonance. By exciting with off-resonant green 520 nm laser and filtering the narrow c-a transition (see Figure 1a) we perform the two-photon interference of single photons from remote  $\text{SnV}^-$  and probe the optical indistinguishability at various detunings.

## II. RESULTS

### Spectral distribution of the resonant transitions in low-strain samples

To minimize lattice damage during defect creation, we implanted ions into the samples along crystal channels, aligning the ions at a  $0^\circ$  incidence angle relative to the [001] diamond surface [44, 45]. This approach reduces implantation-induced defects and yields favorable opti-

cal properties across a range of implantation energies, with lower energies resulting in the least lattice damage. Figures 2a and 2b show results from the 40 keV implanted sample, where we observe a ground state splitting value of 824 GHz and a narrow spectral distribution of zero-phonon lines (ZPLs) with a linewidth variation of  $\sigma \approx 4.0$  GHz, due to a low-strain environment. This sample thus serves as a best-case scenario, exhibiting minimal spectral broadening. For the remaining experiments presented in this study, we focus on samples implanted at 80 keV and 170 keV, as the increased implantation depth places the defects farther from the diamond surface, reducing photoinduced spectral drift effects caused by the strong off-resonant excitation. A forthcoming study will present a comprehensive statistical analysis of channeled implantation across different energies.

### Coherent properties of the electronic transitions under Stark tuning

To enable tuning of defects to account for inhomogeneous broadening, we fabricated a pair of parallel electrodes to create a controlled electric field (see Methods and Figure 3a), allowing us to tune the optical transitions of  $\text{SnV}^-$  centers.

In contrast to prior work by De Santis et al. [43], we identified  $\text{SnV}^-$  centers that maintain optical coherence across a tuning range of up to 4 GHz, as demonstrated by optical Rabi oscillations. Figure 2d shows the autocorrelation functions  $g^{(2)}(\Delta t)$  measured across applied voltages from  $-100$  V to 130 V under resonant excitation with a continuous-wave charge repump laser. Fitting these measurements with a Rabi oscillation model [46] shows preserved optical coherence across a tuning range of 4 GHz, as demonstrated in Figure 2c.

The kink in the Stark shift curve at approximately  $-50$  V (Figure 2c) can be attributed to nearby single or multiple charge traps whose occupancy changes under the applied electric field. As the field strength modulates the traps' energy levels, it reaches a threshold where the traps either capture or release charge carriers, altering the local electric field at the  $\text{SnV}^-$  centre and causing the observed discontinuity. This switching behavior is further influenced by the traps' population fluctuations at higher fields, leading to additional spectral broadening [47, 48]. We model the charge-trap effect with two fourth-order polynomials, corresponding to the traps being filled or empty, as shown by the black dashed fit in Figure 2c.

To further examine the nature of the spectral broadening, we conducted resonant excitation experiments at low powers, omitting the use of the charge repump laser, which can facilitate photoionization of charge traps and induce spectral diffusion [48, 49]. By using only resonant excitation, we preserved near-Fourier-limited linewidths of approximately 40 MHz, within  $\approx 1.5$  times the Fourier limit. The optical linewidths can be further narrowed by decreasing the temperature [50]. We confirmed this

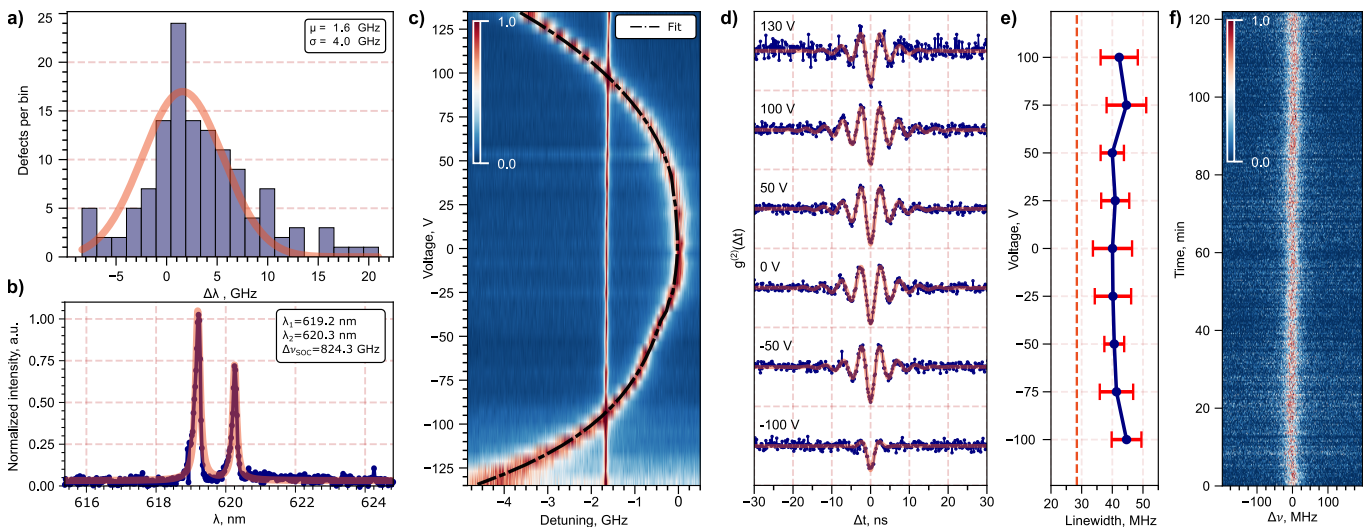


FIG. 2. Statistics of optical properties of obtained colour centers. (a) Histogram of the ZPL distribution for  $\text{SnV}^-$  centers implanted at 40 keV, with a fitted Gaussian curve showing an inhomogeneous broadening of  $\sigma = 4.0$  GHz. The centre of the distribution is offset by  $\mu = 1.6$  GHz from 484.130 THz. (b) Photoluminescence (PL) spectrum showing the distribution of zero-phonon lines (ZPLs) for 110 defects, with two prominent peaks at 619.2 nm and 620.3 nm, corresponding to 824.3 GHz orbital splitting and reduced inhomogeneous broadening, indicating the low-strain environment in ion-implanted samples. (c) Detuning of the optical transition as a function of voltage, showing a tuning range of up to 4 GHz. The straight line is the signal from the second defect in the remote node, showing the control over the spectral overlap. The black dashed curve is the fit function obtained by introducing a two-level system (a charge trap) interacting with the  $\text{SnV}^-$ . (d) The autocorrelation function  $g^{(2)}(\Delta t)$  displays Rabi oscillations at different voltages, indicating that coherent oscillations persist despite Stark tuning. (e) Tuning of the optical transition of the tin-vacancy ( $\text{SnV}^-$ ) centre using an applied electric field at voltages from  $-100$  V to  $100$  V. The linewidths remain near Fourier-limited up to a 1 GHz tuning range. The red dashed line on the side plot marks the Fourier limit of (28.4 MHz) for an emitter with  $T_1 = 5.6$  ns lifetime. (f) The optical transition demonstrated spectral stability, showing a single-scan linewidth of 31.5 MHz and an averaged linewidth of 31.9 MHz over a 2-hour measurement period.

by performing repeated scans with enhanced cooling and thermal shielding in another cryostat, yielding narrower lines from  $\text{SnV}^-$  centers located between the electrodes (Figure 2f). The optical transition remains spectrally stable with a single-scan linewidth of 31.5 MHz and an averaged linewidth of 31.9 MHz over the 2-hour measurement, despite the charge state being reinitialized with the continuous-wave (cw) 520 nm laser.

### Detuning-dependent remote two-photon interference

The broad tuning range and preserved optical coherence allow us to investigate two-photon interference [51, 52] between spatially separated  $\text{SnV}^-$  centers (see Figure 3a) under frequency detuning via the Stark effect.

To capture the detuning-dependent nature of the two-photon interference, the experiment was performed at three voltage setpoints: resonant, moderately detuned, and maximally detuned. For the resonant measurements, the setpoint was selected on a slope of the tuning curve to enable periodic overlap checks of the resonances. Every five minutes, off-resonant excitation was swapped to resonant for overlap verification. The count rate of the zero-phonon lines at the interferometer was set by adjusting the excitation powers to yield 4 kcts/s for each

node. The measured second-order autocorrelation functions ( $g^{(2)}(0)$ ) show the purity of the single photon emission (see Figure 3b) from the  $\text{SnV}^-$  used in this experiment.

The 9 h zero detuning measurement presented in Figure 4a reveals a Hong-Ou-Mandel dip with visible narrowing of the antibunching compared to an ideal case with zero spectral diffusion (black dashed curve in Figure 4a). The interference visibility was measured to be  $V_{\text{HOM}}(0) = 0.80 \pm 0.06$  for the resonant case without any postprocessing. For the moderately detuned case, the tunable optical transitions were shifted to introduce a frequency detuning of 800 MHz between photons. The resulting dip, presented in Figure 4b, shows interference between single photons yielding  $V_{\text{HOM}}(0) = 0.63 \pm 0.08$ .

The maximally detuned case was measured with the setpoint at the maximum allowed voltage of 130 V that did not introduce heating of the cryostat. The resulting autocorrelation function in Figure 4c shows that at maximum detuning, two-photon interference signatures are no longer visible within our experimental detection time resolution – a result of combined large detuning and spectral diffusion measured at high voltage [53, 54].

To model the measured second-order autocorrelation function in the case of two-photon interference [55, 56], we used a theoretical framework that accounts for the

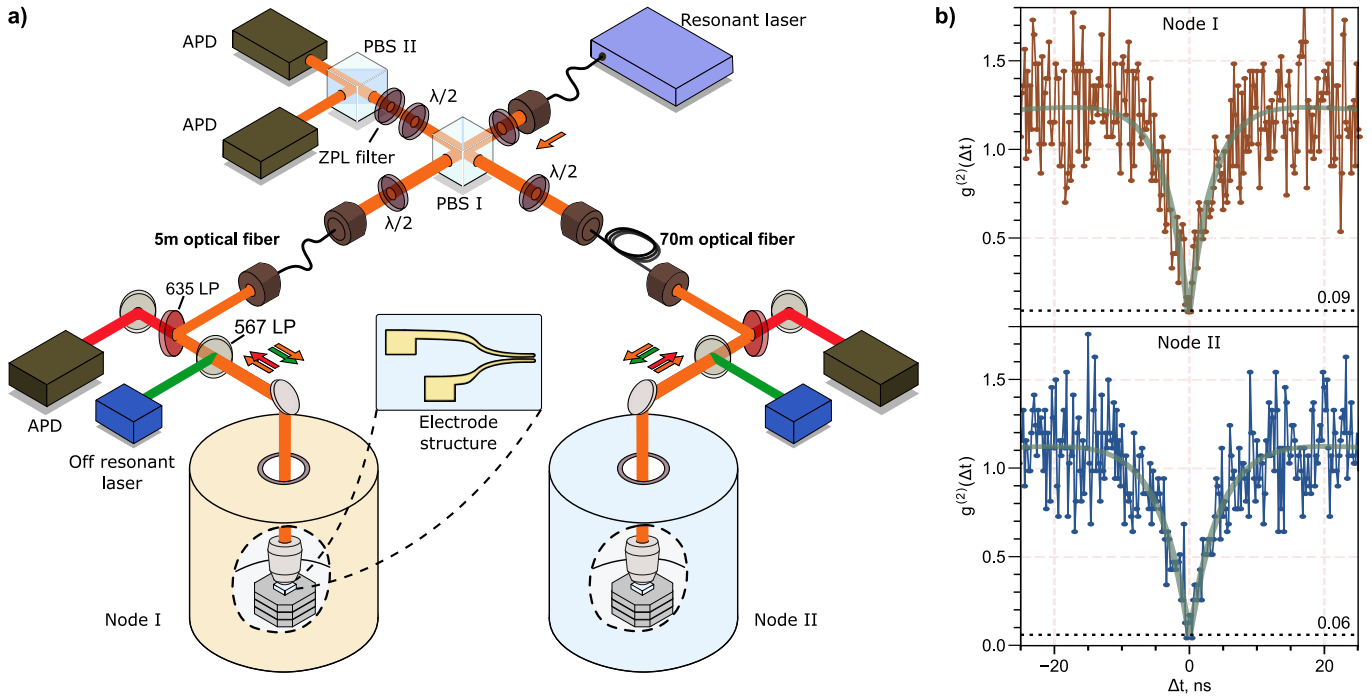


FIG. 3. Two-node tin-vacancy experiment setup. (a) Schematic of the optical setup. The system consists of two cryostats, node I and node II, located in separate rooms and connected by a 70 m long polarization-maintaining (PM) fiber. Off-resonant excitation using a 520 nm laser was employed, with the emission from the tin-vacancy centers filtered by long-pass filters and guided to an interferometer via the fibers. Half-wave plates and polarizing beam splitters were used to control and combine the emission from both nodes. The combined output is filtered with an  $\approx 0.5$  nm broad bandpass filter, and the resulting signal is detected using avalanche photodiodes to measure coincidence counts. (b) Autocorrelation function  $g^{(2)}(\Delta t)$  measured for single defects in both cryostats, confirming that each node contains a single defect with  $g_{\text{I}}^{(2)}(0) \approx 0.09$  and  $g_{\text{II}}^{(2)}(0) \approx 0.05$ .

coherence properties of the emitters and the effects of spectral diffusion (see Methods for details). This model (equation 6) was used to produce the red curve, which fits the experimental data in Figure 4.

### III. DISCUSSION

In this study, we demonstrate the successful generation of  $\text{SnV}^-$  defects with a narrow inhomogeneous distribution without the use of HPHT annealing [41]. Although HPHT annealing effectively reduces inhomogeneous broadening, it can significantly degrade surface quality, making it less compatible with nanofabrication. By employing channeled implantation, we achieved a narrow inhomogeneous distribution for  $\text{SnV}^-$  centers. Defects in these samples exhibited highly coherent optical transitions and long-term spectral stability, even under off-resonant excitation. In the absence of internal stress within the diamond lattice, caused by lattice damage [42], tin vacancies remain unpolarized, making them less susceptible to electric field fluctuations [57, 58].

Furthermore, the obtained narrow inhomogeneous distribution was compensated for by Stark shift tuning, which preserved optical coherence and photon emission quality. This tuning approach, unlike strain-based meth-

ods [59, 60], allows for precise emission frequency alignment with minimal induced dipole moment in the defect, maintaining spectral stability.

We demonstrated two-photon interference experiments between negatively charged tin-vacancy ( $\text{SnV}^-$ ) centers in separate quantum nodes, achieving a visibility of  $80 \pm 6\%$  at zero detuning. The measured high visibility illustrates the high optical coherence of  $\text{SnV}^-$  centers despite off-resonant excitation. The observed spectral diffusion aligns with the presence of a nearby charge trap or multiple traps, as evidenced by the fitted kink in the presented Stark shift measurements in Figure 2c. These findings suggest that the off-resonant excitation approach for single-photon generation is suboptimal, since it induces population fluctuations of the charge traps in the defect's vicinity. Resonant excitation is preferable, since it would selectively excite the  $\text{SnV}^-$ , yielding Fourier-limited emission, thereby maximizing the interference probability [54, 61].

In our detuned interference measurements, we observe that two-photon interference remains feasible even when the photons are not in resonance. The interference in the detuned case is possible because the coherence time of the emitted photons is sufficiently long to exceed the detection time resolution [55, 62–64]. Notably, the interference occurs at the detection stage rather than at

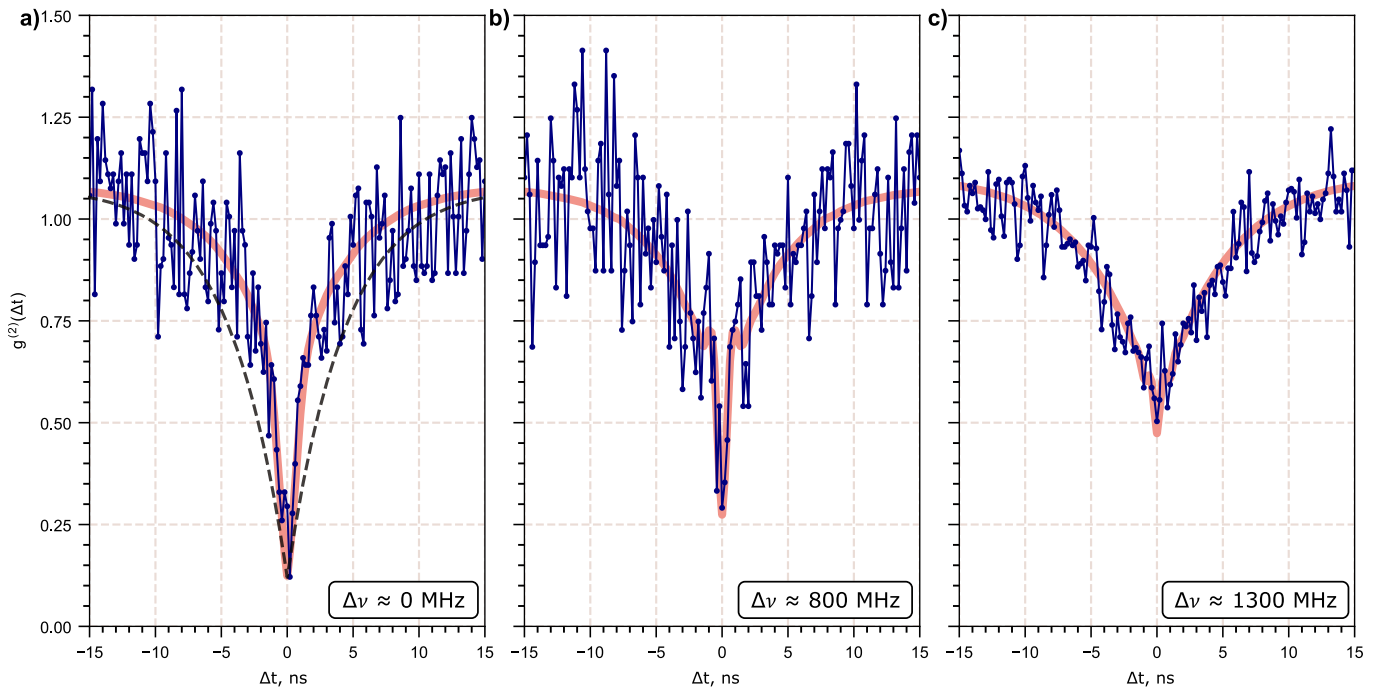


FIG. 4. Detuning-dependent two-photon interference of single photons emitted from two remote tin-vacancy centers. The second-order cross-correlation function  $g^{(2)}(\Delta t)$  is measured at three detuning points: (a) resonant condition with  $\Delta\nu \approx 0$  MHz, (b) moderate detuning with  $\Delta\nu \approx 800$  MHz, and (c) maximum detuning with  $\Delta\nu \approx 1300$  MHz. The blue points represent the recorded data. The red curve is the fit with equation 6 for two-photon interference for indistinguishable sources with varying detunings and spectral diffusion. The black dashed curve in (a) represents the simulation of the ideal resonant case using the same parameters as the fit to the experimental data, except with zero spectral diffusion. The observed Hong-Ou-Mandel dips reveal the two-photon interference even at large detunings, with narrowing interference signatures due to spectral diffusion. Despite the induced spectral diffusion, the interference visibility in resonance was measured to be  $V_{\text{HOM}}(0) = 0.80 \pm 0.06$  and  $V_{\text{HOM}}(0) = 0.63 \pm 0.08$  at moderate detuning. At maximum detuning, the interference features are washed out due to the combined effects of large detuning and enhanced spectral diffusion.

the beam splitter, with the measurement time bin acting as a temporal filter. This filter broadens the observed frequency resolution to  $\frac{2\pi}{\Delta\tau}$ , effectively "erasing" the which-frequency information [65]. Furthermore, such detuned interference can be useful for entangling photons of different colors [66], enabling the creation of entangled states between non-identical quantum systems [67]. In conclusion, this study establishes SnV<sup>-</sup> centers as a scalable, promising platform for quantum networking. The generation of SnV<sup>-</sup> centers with narrow inhomogeneous distribution, combined with Stark tuning and robust two-photon interference, positions these centers as key candidates for large-scale quantum applications.

## ACKNOWLEDGMENTS

We acknowledge fruitful discussions with Florian Kaiser, Jonathan Körber, Rainer Stöhr, Javid Javazade, and Roman Kolesov. This work was funded by the Spinning project (BMBF, No. 13N16219), QR.X project (BMBF, No. 16KISQ013), by the European Union via SPINUS, by the German Research Foundation (DFG, No. RTG 2642), and the state of Baden-Württemberg

(QC4BW and KQCBW24). O.B. acknowledges support from the RTG 2642.

## APPENDICES

### A. Experimental setup

The two-node setup includes two cryostats, the AttoDry800 (node I) and Bluefors LD250 (node II) (see Figure 3a), located in separate rooms and connected by a 70 m long polarization-maintaining (PM) fiber. The setup directs the green excitation beam through a 567 nm long-pass filter into the cryostat, where it is focused by a 0.9 NA, 100 $\times$  objective (Olympus MPLN). Emission from the SnV<sup>-</sup> is then separated by a 630 nm long-pass filter, guiding the phonon sideband and coherent zero-phonon line emission to the avalanche photodiodes (APDs) (SPCM-AQRH-14-FC, Excelitas Technologies Corp.). The zero-phonon lines are collected via a 70 m PM fiber for node I and a 5 m PM fiber for node II, and then coupled into an interferometer. Inside the interferometer, emission from both nodes is combined into a single spatial mode with orthogonal polarizations using



half-wave plates and a polarizing beam splitter (PBS I). This mode is further filtered by a tilted 0.5 nm narrow-band-pass filter (LC-HBP630.2/0.5, Alluxa, Inc.), isolating the desired line. Due to the substantial spectral separation between emission lines stemming from large spin-orbit coupling, a narrow etalon is not required, which allows for coherent transition selection with a commercial spectral filter. The combined and filtered emission is split again by a second polarizing beam splitter. This configuration allows two modes of operation: (1) with a half-wave plate before PBS II maintaining separate polarizations, enabling independent measurements from nodes I and II; and (2) with the half-wave plate rotated by  $45^\circ$ , mixing polarizations to observe interference [68].

The measured photon arrival times are analyzed using time-stamping electronics (Timetagger 20, Swabian Instruments), allowing precise time-correlation measurements. Additionally, a resonant laser ( $620 \pm 10$  nm DLC TA-SHG PRO, TOPTICA Photonics AG) is introduced into the setup through PBS I, coupling into the PM fibers of both nodes. This design allows the collected zero-phonon line emission (from green excitation) to share the spatial mode with the resonant laser, enabling clear identification of defects under both off-resonant and resonant excitation conditions. The remote control of both nodes was performed using Qudi software with customized modules [69].

## B. Sample fabrication

In this work, we implanted tin ions into [001]-oriented CVD-grown diamond at energies of 40 keV, 80 keV, and 170 keV at a  $0^\circ$  incident angle and  $5 \times 10^{10} \text{ cm}^{-2}$ . Following implantation, high-temperature annealing at  $1500^\circ\text{C}$  was performed for 1 hour. As a final step, 3-acid boiling was employed for 3 hours to remove the graphitized surface layer.

## C. Electrodes fabrication

The electrodes are spaced  $1.7 \mu\text{m}$  apart and are  $1.8 \mu\text{m}$  wide. They were created using a liftoff process, with the electrode shape patterned into a double layer of photoresist (LOR3A and Shipley S1805) via optical lithography. The shape begins as two narrow, parallel electrodes that gradually widen and separate until they terminate in wire-bonding pads. The patterned shape is slightly narrower and farther apart than the final electrodes. These adjustments help to prevent the electrodes from fusing due to the proximity effect. Following the patterning, 10 nm of Cr as a mating layer, followed by 100 nm of Au, were deposited onto the sample by e-beam evaporation at a rate of  $1 \text{ \AA s}^{-1}$ . The remaining photoresist was dissolved in N-Methyl-2-pyrrolidone (NMP), which lifts off the unwanted gold, leaving just the electrodes depicted in Figure 3a.

## D. Modeling the Stark shift

To model the observed kink in the Stark shift curve caused by a nearby charge trap, we consider the following higher-order polynomial terms [43] in the spectral shift of the defect:

$$h\Delta\nu_{\pm}(\mathcal{E}) = -\mu_{\text{tin}}(\mathcal{E} \pm \mathcal{E}_{\text{trap}}) - \frac{\alpha}{2}(\mathcal{E} \pm \mathcal{E}_{\text{trap}})^2 - \frac{\beta}{6}(\mathcal{E} \pm \mathcal{E}_{\text{trap}})^3 - \frac{\gamma}{24}(\mathcal{E} \pm \mathcal{E}_{\text{trap}})^4, \quad (1)$$

where  $\mathcal{E}$  is the applied voltage combined with the static internal electric field (*i.e.*, strain or surface-induced),  $\alpha$ ,  $\beta$ , and  $\gamma$  represent the second-, third-, and fourth-order Stark coefficients, respectively, and  $\mu$  is the linear Stark coefficient. The term  $\mathcal{E}_{\text{trap}}$  denotes the electric field offset from the charge trap in the defect's vicinity.

To account for the probability  $p$  of the trap flipping in response to the applied field, we follow the definition by Segura et al.[47]:

$$p = 1 / \left[ 1 + \exp\left(\frac{A_0 + 2\mu_{\text{trap}}\mathcal{E}}{k_{\text{B}}T}\right) \right], \quad (2)$$

where  $\mu_{\text{trap}}$  is the charge trap's dipole moment,  $A_0$  represents the external field dependence of the charge trap population.

The combined spectral shift, considering both filled and empty states of the trap, is then expressed as:

$$h\Delta\nu_{\text{total}}(\mathcal{E}) = p \cdot h\Delta\nu_{+}(\mathcal{E}) + (1 - p) \cdot h\Delta\nu_{-}(\mathcal{E}). \quad (3)$$

Here,  $h\Delta\nu_{+}(\mathcal{E})$  and  $h\Delta\nu_{-}(\mathcal{E})$  represent the Stark shifts when the trap is in the filled and empty states, respectively. The resulting spectral shift  $h\Delta\nu_{\text{total}}(\mathcal{E})$  captures the overall behavior observed in the experimental data (black curve fit in Figure 2c), showing a kink at the point where the trap transitions between states.

## E. Modeling of two-photon interference

To model the measured second-order cross-correlation function in the case of two-photon interference, we use the expression for  $g_{\text{tpti}}^{(2)}(\tau)$  as described in [56]:

$$g_{\text{tpti}}^{(2)}(\tau) = c_1^2 g_{11}^{(2)}(\tau) + c_2^2 g_{22}^{(2)}(\tau) + 2c_1 c_2 \left\{ 1 - \eta \frac{S_1 S_2}{I_1 I_2} \left| g_{11}^{(1)}(\tau) \right| \left| g_{22}^{(1)}(\tau) \right| \cos(\Delta\omega\tau) \right\}, \quad (4)$$

where  $c_i = \frac{I_i}{I_1 + I_2}$  represents the normalized intensity ratio of source  $i$ ,  $g_{ii}^{(2)}(\tau)$  is the second-order autocorrelation function of source  $i$ ,  $g_{ii}^{(1)}(\tau)$  is the first-order autocorrelation function of source  $i$ ,  $\eta$  is a visibility reduction

factor accounting for experimental factors such as classical interferometer visibility,  $S_i$  is the signal count rate from source  $i$ ,  $I_i$  is the total detected count rate from source  $i$ , including background,  $\Delta\omega = \omega_1 - \omega_2$  is the frequency detuning between the two sources,  $\tau$  is the time delay between photon detection events.

The first two terms in equation 4 represent the second-order autocorrelations of each individual source. The third term accounts for the interference between the two sources, depending on their coherence properties and the frequency detuning  $\Delta\omega$ .

For a quantum emitter under continuous excitation, the magnitude of the first-order autocorrelation function describes the decay of coherence over time due to dephasing processes:

$$\left| g_{ii}^{(1)}(\tau) \right| = e^{-\gamma\tau/2}, \quad (5)$$

where  $\gamma = \frac{1}{\tau_{\text{coh}}}$  is the homogeneous linewidth of the

emitter, and  $\tau_{\text{coh}}$  is the coherence time of the emitter. The extent of coherence of the source can be estimated by how closely the emitter linewidth approaches the Fourier limit. In the case of transform-limited lines, the coherence time reaches its maximum value,  $\tau_{\text{coh}} = 2\tau_{\text{rad}}$ , which is twice the radiative lifetime [46].

In the presence of spectral diffusion, the beating signal described by equation 4 becomes washed out due to contributions from multiple beating frequencies. To account for spectral diffusion, we modify the function accordingly. Assuming a Gaussian distribution for the detuning variations, the modified function can be expressed as a convolution:

$$g_{\text{sd}}^{(2)}(\tau) = \int_{-\infty}^{\infty} \mathcal{G}_{\sigma}(\Delta\omega') g_{\text{tpti}}^{(2)}(\tau, \Delta\omega') d\Delta\omega', \quad (6)$$

where  $\mathcal{G}_{\sigma}(\Delta\omega')$  is the Gaussian kernel characterizing the spectral diffusion,  $\sigma$  is the standard deviation of the frequency distribution caused by spectral diffusion, and  $\omega_0$  is the central frequency.

- 
- [1] D. Awschalom, K. K. Berggren, H. Bernien, S. Bhave, L. D. Carr, P. Davids, S. E. Economou, D. Englund, A. Faraon, M. Fejer, S. Guha, M. V. Gustafsson, E. Hu, L. Jiang, J. Kim, B. Korzh, P. Kumar, P. G. Kwiat, M. Lončar, M. D. Lukin, D. A. Miller, C. Monroe, S. W. Nam, P. Narang, J. S. Orcutt, M. G. Raymer, A. H. Safavi-Naeini, M. Spiropulu, K. Srinivasan, S. Sun, J. Vučković, E. Waks, R. Walsworth, A. M. Weiner, and Z. Zhang, Development of Quantum Interconnects (QuICs) for Next-Generation Information Technologies, PRX Quantum **2**, 017002 (2021), publisher: American Physical Society.
- [2] S. Ritter, C. Nölleke, C. Hahn, A. Reiserer, A. Neuzner, M. Uphoff, M. Mücke, E. Figueroa, J. Bochmann, and G. Rempe, An elementary quantum network of single atoms in optical cavities, Nature **484**, 195 (2012).
- [3] J. Hofmann, M. Krug, N. Ortegel, L. Gérard, M. Weber, W. Rosenfeld, and H. Weinfurter, Heralded Entanglement Between Widely Separated Atoms, Science **337**, 72 (2012).
- [4] M. Bock, P. Eich, S. Kucera, M. Kreis, A. Lenhard, C. Becher, and J. Eschner, High-fidelity entanglement between a trapped ion and a telecom photon via quantum frequency conversion, Nature Communications **9**, 1998 (2018).
- [5] A. Reiserer, N. Kalb, G. Rempe, and S. Ritter, A quantum gate between a flying optical photon and a single trapped atom, Nature **508**, 237 (2014), publisher: Nature Publishing Group.
- [6] D. Hucul, I. V. Inlek, G. Vittorini, C. Crocker, S. Deb-nath, S. M. Clark, and C. Monroe, Modular entanglement of atomic qubits using photons and phonons, Nature Physics **11**, 37 (2015), publisher: Nature Publishing Group.
- [7] W. Rosenfeld, D. Burchardt, R. Garthoff, K. Redeker, N. Ortegel, M. Rau, and H. Weinfurter, Event-Ready Bell Test Using Entangled Atoms Simultaneously Closing Detection and Locality Loopholes, Physical Review Letters **119**, 010402 (2017).
- [8] L. Zaporski, N. Shofer, J. H. Bodey, S. Manna, G. Gillard, M. H. Appel, C. Schimpf, S. F. Covre Da Silva, J. Jarman, G. Delamare, G. Park, U. Haeusler, E. A. Chekhovich, A. Rastelli, D. A. Gangloff, M. Atatüre, and C. Le Gall, Ideal refocusing of an optically active spin qubit under strong hyperfine interactions, Nature Nanotechnology **18**, 257 (2023).
- [9] Y. Yu, S. Liu, C.-M. Lee, P. Michler, S. Reitzenstein, K. Srinivasan, E. Waks, and J. Liu, Telecom-band quantum dot technologies for long-distance quantum networks, Nature Nanotechnology **18**, 1389 (2023).
- [10] P. Siyushev, G. Stein, J. Wrachtrup, and I. Gerhardt, Molecular photons interfaced with alkali atoms, Nature **509**, 66 (2014).
- [11] D. Lago-Rivera, S. Grandi, J. V. Rakonjac, A. Seri, and H. de Riedmatten, Telecom-heralded entanglement between multimode solid-state quantum memories, Nature **594**, 37 (2021), publisher: Nature Publishing Group.
- [12] A. Ruskuc, C.-J. Wu, E. Green, S. L. Hermans, J. Choi, and A. Faraon, Scalable multipartite entanglement of remote rare-earth ion qubits, arXiv preprint arXiv:2402.16224 (2024).
- [13] P. Kurpiers, P. Magnard, T. Walter, B. Royer, M. Pechal, J. Heinsoo, Y. Salathé, A. Akin, S. Storz, J.-C. Besse, S. Gasparinetti, A. Blais, and A. Wallraff, Deterministic quantum state transfer and remote entanglement using microwave photons, Nature **558**, 264 (2018), publisher: Nature Publishing Group.
- [14] B. Hensen, H. Bernien, A. E. Dréau, A. Reiserer, N. Kalb, M. S. Blok, J. Ruitenber, R. F. L. Vermeulen, R. N. Schouten, C. Abellán, W. Amaya, V. Pruneri, M. W. Mitchell, M. Markham, D. J. Twitchen, D. Elkouss, S. Wehner, T. H. Taminiau, and R. Hanson, Loophole-

- free Bell inequality violation using electron spins separated by 1.3 kilometres, *Nature* **526**, 682 (2015), publisher: Nature Publishing Group.
- [15] D. D. Awschalom, R. Hanson, J. Wrachtrup, and B. B. Zhou, Quantum technologies with optically interfaced solid-state spins, *Nature Photonics* **12**, 516 (2018).
- [16] D. B. Higginbottom, A. T. Kurkjian, C. Chartrand, M. Kazemi, N. A. Brunelle, E. R. MacQuarrie, J. R. Klein, N. R. Lee-Hone, J. Stacho, M. Ruether, *et al.*, Optical observation of single spins in silicon, *Nature* **607**, 266 (2022).
- [17] N. Morioka, C. Babin, R. Nagy, I. Gediz, E. Hesselmeier, D. Liu, M. Joliffe, M. Niethammer, D. Dasari, V. Vorobyov, *et al.*, Spin-controlled generation of indistinguishable and distinguishable photons from silicon vacancy centres in silicon carbide, *Nature communications* **11**, 2516 (2020).
- [18] R.-Z. Fang, X.-Y. Lai, T. Li, R.-Z. Su, B.-W. Lu, C.-W. Yang, R.-Z. Liu, Y.-K. Qiao, C. Li, Z.-G. He, *et al.*, Experimental generation of spin-photon entanglement in silicon carbide, *Physical Review Letters* **132**, 160801 (2024).
- [19] C. Nguyen, D. Sukachev, M. Bhaskar, B. Machielse, D. Levonian, E. Knall, P. Stroganov, C. Chia, M. Burek, R. Riedinger, *et al.*, An integrated nanophotonic quantum register based on silicon-vacancy spins in diamond, *Physical Review B* **100**, 165428 (2019).
- [20] C. M. Knaut, A. Suleymanzade, Y.-C. Wei, D. R. Assumpcao, P.-J. Stas, Y. Q. Huan, B. Machielse, E. N. Knall, M. Sutula, G. Baranes, N. Sinclair, C. De-Eknamkul, D. S. Levonian, M. K. Bhaskar, H. Park, M. Lončar, and M. D. Lukin, Entanglement of nanophotonic quantum memory nodes in a telecom network, *Nature* **629**, 573 (2024), publisher: Nature Publishing Group.
- [21] D. D. Sukachev, A. Sipahigil, C. T. Nguyen, M. K. Bhaskar, R. E. Evans, F. Jelezko, and M. D. Lukin, Silicon-vacancy spin qubit in diamond: a quantum memory exceeding 10 ms with single-shot state readout, *Physical review letters* **119**, 223602 (2017).
- [22] P.-J. Stas, Y. Q. Huan, B. Machielse, E. N. Knall, A. Suleymanzade, B. Pingault, M. Sutula, S. W. Ding, C. M. Knaut, D. R. Assumpcao, Y.-C. Wei, M. K. Bhaskar, R. Riedinger, D. D. Sukachev, H. Park, M. Lončar, D. S. Levonian, and M. D. Lukin, Robust multi-qubit quantum network node with integrated error detection, *Science* **378**, 557 (2022), publisher: American Association for the Advancement of Science.
- [23] C. Hepp, T. Müller, V. Waselowski, J. N. Becker, B. Pingault, H. Sternschulte, D. Steinmüller-Nethl, A. Gali, J. R. Maze, M. Atatüre, and C. Becher, Electronic Structure of the Silicon Vacancy Color Center in Diamond, *Physical Review Letters* **112**, 036405 (2014), publisher: American Physical Society.
- [24] G. Thiering and A. Gali, *Ab Initio* Magneto-Optical Spectrum of Group-IV Vacancy Color Centers in Diamond, *Physical Review X* **8**, 021063 (2018).
- [25] A. Sipahigil, R. E. Evans, D. D. Sukachev, M. J. Burek, J. Borregaard, M. K. Bhaskar, C. T. Nguyen, J. L. Pacheco, H. A. Atikian, C. Meuwly, R. M. Camacho, F. Jelezko, E. Bielejec, H. Park, M. Lončar, and M. D. Lukin, An integrated diamond nanophotonics platform for quantum-optical networks, *Science* **354**, 847 (2016).
- [26] R. E. Evans, A. Sipahigil, D. D. Sukachev, A. S. Zibrov, and M. D. Lukin, Narrow-linewidth homogeneous optical emitters in diamond nanostructures via silicon ion implantation, *Physical Review Applied* **5**, 044010 (2016).
- [27] T. Schröder, M. E. Trusheim, M. Walsh, L. Li, J. Zheng, M. Schukraft, A. Sipahigil, R. E. Evans, D. D. Sukachev, C. T. Nguyen, *et al.*, Scalable focused ion beam creation of nearly lifetime-limited single quantum emitters in diamond nanostructures, *Nature communications* **8**, 15376 (2017).
- [28] A. Sipahigil, K. Jahnke, L. Rogers, T. Teraji, J. Isoya, A. Zibrov, F. Jelezko, and M. Lukin, Indistinguishable Photons from Separated Silicon-Vacancy Centers in Diamond, *Physical Review Letters* **113**, 113602 (2014).
- [29] M. K. Bhaskar, R. Riedinger, B. Machielse, D. S. Levonian, C. T. Nguyen, E. N. Knall, H. Park, D. Englund, M. Lončar, D. D. Sukachev, and M. D. Lukin, Experimental demonstration of memory-enhanced quantum communication, *Nature* **580**, 60 (2020).
- [30] K. D. Jahnke, A. Sipahigil, J. M. Binder, M. W. Doherty, M. Metsch, L. J. Rogers, N. B. Manson, M. D. Lukin, and F. Jelezko, Electron-phonon processes of the silicon-vacancy centre in diamond, *New Journal of Physics* **17**, 043011 (2015).
- [31] D. Sukachev, A. Sipahigil, C. Nguyen, M. Bhaskar, R. Evans, F. Jelezko, and M. Lukin, Silicon-Vacancy Spin Qubit in Diamond: A Quantum Memory Exceeding 10 ms with Single-Shot State Readout, *Physical Review Letters* **119**, 223602 (2017), publisher: American Physical Society.
- [32] P. Siyushev, M. H. Metsch, A. Ijaz, J. M. Binder, M. K. Bhaskar, D. D. Sukachev, A. Sipahigil, R. E. Evans, C. T. Nguyen, M. D. Lukin, P. R. Hemmer, Y. N. Palyanov, I. N. Kupriyanov, Y. M. Borzdov, L. J. Rogers, and F. Jelezko, Optical and microwave control of germanium-vacancy center spins in diamond, *Physical Review B* **96**, 081201 (2017).
- [33] T. Iwasaki, Y. Miyamoto, T. Taniguchi, P. Siyushev, M. H. Metsch, F. Jelezko, and M. Hatano, Tin-Vacancy Quantum Emitters in Diamond, *Physical Review Letters* **119**, 253601 (2017).
- [34] M. E. Trusheim, B. Pingault, N. H. Wan, M. Gündoğan, L. De Santis, R. Debroux, D. Gangloff, C. Purser, K. C. Chen, M. Walsh, J. J. Rose, J. N. Becker, B. Lienhard, E. Bersin, I. Paradeisanos, G. Wang, D. Lyzwa, A. R.-P. Montblanch, G. Malladi, H. Bakhrū, A. C. Ferrari, I. A. Walmsley, M. Atatüre, and D. Englund, Transform-Limited Photons From a Coherent Tin-Vacancy Spin in Diamond, *Physical Review Letters* **124**, 023602 (2020).
- [35] K. Senkalla, G. Genov, M. H. Metsch, P. Siyushev, and F. Jelezko, Germanium Vacancy in Diamond Quantum Memory Exceeding 20 ms, *Physical Review Letters* **132**, 026901 (2024).
- [36] M. Zahedian, V. Vorobyov, and J. Wrachtrup, Blueprint for efficient nuclear spin characterization with color centers, *Physical Review B* **109**, 214111 (2024).
- [37] X. Guo, A. M. Stramma, Z. Li, W. G. Roth, B. Huang, Y. Jin, R. A. Parker, J. Arjona Martínez, N. Shofer, C. P. Michaels, C. P. Purser, M. H. Appel, E. M. Alexeev, T. Liu, A. C. Ferrari, D. D. Awschalom, N. Deleegan, B. Pingault, G. Galli, F. J. Heremans, M. Atatüre, and A. A. High, Microwave-Based Quantum Control and Coherence Protection of Tin-Vacancy Spin Qubits in a Strain-Tuned Diamond-Membrane Heterostructure, *Physical Review X* **13**, 041037 (2023).



- [38] E. I. Rosenthal, C. P. Anderson, H. C. Kleidermacher, A. J. Stein, H. Lee, J. Grzesik, G. Scuri, A. E. Rugar, D. Riedel, S. Aghaeimeibodi, G. H. Ahn, K. Van Gasse, and J. Vučković, Microwave Spin Control of a Tin-Vacancy Qubit in Diamond, *Physical Review X* **13**, 031022 (2023).
- [39] I. Karapatzakis, J. Resch, M. Schrodin, P. Fuchs, M. Kieschnick, J. Heupel, L. Kussi, C. Sürgers, C. Popov, J. Meijer, C. Becher, W. Wernsdorfer, and D. Hunger, Microwave Control of the Tin-Vacancy Spin Qubit in Diamond with a Superconducting Waveguide, *Physical Review X* **14**, 031036 (2024).
- [40] L. Li, L. D. Santis, I. B. W. Harris, K. C. Chen, Y. Gao, I. Christen, H. Choi, M. Trusheim, Y. Song, C. Errando-Herranz, J. Du, Y. Hu, G. Clark, M. I. Ibrahim, G. Gilbert, R. Han, and D. Englund, Heterogeneous integration of spin-photon interfaces with a CMOS platform, *Nature* **630**, 70 (2024), publisher: Nature Publishing Group.
- [41] Y. Narita, P. Wang, K. Ikeda, K. Oba, Y. Miyamoto, T. Taniguchi, S. Onoda, M. Hatano, and T. Iwasaki, Multiple Tin-Vacancy Centers in Diamond with Nearly Identical Photon Frequency and Linewidth, *Physical Review Applied* **19**, 024061 (2023).
- [42] S. Aghaeimeibodi, D. Riedel, A. E. Rugar, C. Dory, and J. Vučković, Electrical Tuning of Tin-Vacancy Centers in Diamond, *Physical Review Applied* **15**, 064010 (2021).
- [43] L. De Santis, M. E. Trusheim, K. C. Chen, and D. R. Englund, Investigation of the Stark Effect on a Centrosymmetric Quantum Emitter in Diamond, *Physical Review Letters* **127**, 147402 (2021).
- [44] O. Lehtinen, B. Naydenov, P. Börner, K. Melentjevic, C. Müller, L. P. McGuinness, S. Pezzagna, J. Meijer, U. Kaiser, and F. Jelezko, Molecular dynamics simulations of shallow nitrogen and silicon implantation into diamond, *Physical Review B* **93**, 035202 (2016).
- [45] S. Santonocito, A. Denisenko, M. Schreck, A. Pasquarelli, and J. Wrachtrup, Suppression of thermal diffusion of vacancies across p-n junction structures in diamond. Application to SnV centers by ion implantation, *New Journal of Physics* **26**, 053036 (2024).
- [46] Y. Wang, V. Bushmakina, G. A. Stein, A. W. Schell, and I. Gerhardt, Optical Ramsey spectroscopy on a single molecule, *Optica* **9**, 374 (2022).
- [47] J. M. Segura, G. Zumofen, A. Renn, B. Hecht, and U. P. Wild, Tip-induced spectral dynamics of single molecules, *Chemical Physics Letters* **340**, 77 (2001).
- [48] L. C. Bassett, F. J. Heremans, C. G. Yale, B. B. Buckley, and D. D. Awschalom, Electrical Tuning of Single Nitrogen-Vacancy Center Optical Transitions Enhanced by Photoinduced Fields, *Physical Review Letters* **107**, 266403 (2011).
- [49] J. Görlitz, D. Herrmann, G. Thiering, P. Fuchs, M. Gandil, T. Iwasaki, T. Taniguchi, M. Kieschnick, J. Meijer, M. Hatano, A. Gali, and C. Becher, Spectroscopic investigations of negatively charged tin-vacancy centres in diamond, *New Journal of Physics* **22**, 013048 (2020).
- [50] P. Wang, L. Kazak, K. Senkalla, P. Siyushev, R. Abe, T. Taniguchi, S. Onoda, H. Kato, T. Makino, M. Hatano, F. Jelezko, and T. Iwasaki, Transform-Limited Photon Emission from a Lead-Vacancy Center in Diamond above 10 K, *Physical Review Letters* **132**, 073601 (2024).
- [51] C. K. Hong, Z. Y. Ou, and L. Mandel, Measurement of subpicosecond time intervals between two photons by interference, *Physical Review Letters* **59**, 2044.
- [52] Y. H. Shih and C. O. Alley, New type of einstein-podolsky-rosen-bohm experiment using pairs of light quanta produced by optical parametric down conversion, *Physical Review Letters* **61**, 2921.
- [53] N. Morioka, C. Babin, R. Nagy, I. Gediz, E. Hesselmeier, D. Liu, M. Joliffe, M. Niethammer, D. Dasari, V. Vorobyov, R. Kolesov, R. Stöhr, J. Ul-Hassan, N. T. Son, T. Ohshima, P. Udvarhelyi, G. Thiering, A. Gali, J. Wrachtrup, and F. Kaiser, Spin-controlled generation of indistinguishable and distinguishable photons from silicon vacancy centres in silicon carbide, *Nature Communications* **11**, 2516 (2020).
- [54] M. Rezai, J. Wrachtrup, and I. Gerhardt, Coherence Properties of Molecular Single Photons for Quantum Networks, *Physical Review X* **8**, 031026 (2018).
- [55] T. Legero, T. Wilk, M. Hennrich, G. Rempe, and A. Kuhn, Quantum Beat of Two Single Photons, *Physical Review Letters* **93**, 070503 (2004).
- [56] R. Lettow, Y. L. A. Rezus, A. Renn, G. Zumofen, E. Ikonen, S. Götzinger, and V. Sandoghdar, Quantum Interference of Tunably Indistinguishable Photons from Remote Organic Molecules, *Physical Review Letters* **104**, 123605 (2010), publisher: American Physical Society.
- [57] Z. Li, X. Guo, Y. Jin, F. Andreoli, A. Bilgin, D. D. Awschalom, N. Deegan, F. J. Heremans, D. Chang, G. Galli, and A. A. High, Atomic optical antennas in solids, *Nature Photonics* **18**, 1113 (2024).
- [58] G. Pieplow, C. G. Torun, J. H. D. Munns, F. M. Herrmann, A. Thies, T. Pregolato, and T. Schröder, Quantum Electrometer for Time-Resolved Material Science at the Atomic Lattice Scale (2024), arXiv:2401.14290.
- [59] B. Machielse, S. Bogdanovic, S. Meesala, S. Gauthier, M. Burek, G. Joe, M. Chalupnik, Y. Sohn, J. Holzgrafe, R. Evans, C. Chia, H. Atikian, M. Bhaskar, D. Sukachev, L. Shao, S. Maity, M. Lukin, and M. Lončar, Quantum Interference of Electromechanically Stabilized Emitters in Nanophotonic Devices, *Physical Review X* **9**, 031022 (2019).
- [60] N. H. Wan, T.-J. Lu, K. C. Chen, M. P. Walsh, M. E. Trusheim, L. De Santis, E. A. Bersin, I. B. Harris, S. L. Mouradian, I. R. Christen, E. S. Bielejec, and D. Englund, Large-scale integration of artificial atoms in hybrid photonic circuits, *Nature* **583**, 226 (2020), publisher: Nature Publishing Group.
- [61] B. Kambs and C. Becher, Limitations on the indistinguishability of photons from remote solid state sources, *New Journal of Physics* **20**, 115003 (2018).
- [62] T. B. Pittman, D. V. Strekalov, A. Migdall, M. H. Rubin, A. V. Sergienko, and Y. H. Shih, Can Two-Photon Interference be Considered the Interference of Two Photons?, *Physical Review Letters* **77**, 1917 (1996).
- [63] T. Legero, T. Wilk, A. Kuhn, and G. Rempe, Time-resolved two-photon quantum interference, *Applied Physics B* **77**, 797 (2003).
- [64] M. Halder, A. Beveratos, N. Gisin, V. Scarani, C. Simon, and H. Zbinden, Entangling independent photons by time measurement, *Nature Physics* **3**, 692 (2007), publisher: Nature Publishing Group.
- [65] J. A. Wheeler, The “Past” and the “Delayed-Choice” Double-Slit Experiment, in *Mathematical Foundations of Quantum Theory*, edited by A. R. Marlow (Academic Press, 1978) pp. 9–48.

- [66] T.-M. Zhao, H. Zhang, J. Yang, Z.-R. Sang, X. Jiang, X.-H. Bao, and J.-W. Pan, Entangling Different-Color Photons via Time-Resolved Measurement and Active Feed Forward, *Physical Review Letters* **112**, 103602 (2014).
- [67] R. A. Parker, J. Arjona Martínez, K. C. Chen, A. M. Stramma, I. B. Harris, C. P. Michaels, M. E. Trusheim, M. Hayhurst Appel, C. M. Purser, W. G. Roth, D. Englund, and M. Atatüre, A diamond nanophotonic interface with an optically accessible deterministic electronuclear spin register, *Nature Photonics* **18**, 156 (2024), publisher: Nature Publishing Group.
- [68] J. Beugnon, M. P. A. Jones, J. Dingjan, B. Darquié, G. Messin, A. Browaeys, and P. Grangier, Quantum interference between two single photons emitted by independently trapped atoms, *Nature* **440**, 779 (2006).
- [69] J. M. Binder, A. Stark, N. Tomek, J. Scheuer, F. Frank, K. D. Jahnke, C. Müller, S. Schmitt, M. H. Metsch, T. Unden, T. Gehring, A. Huck, U. L. Andersen, L. J. Rogers, and F. Jelezko, Qudi: A modular python suite for experiment control and data processing, *SoftwareX* **6**, 85 (2017).